

A Solid-State and Flexible Supercapacitor that Operates Across a Wide Temperature Range

Ardalan Chaichi^{1,†}, Gokul Venugopalan^{2,†}, Ram Devireddy¹, Christopher Arges^{2,*},

Manas Ranjan Gartia^{1,*}

¹Department of Mechanical Engineering, Louisiana State University, Baton Rouge, USA 70803

²Cain Department of Chemical Engineering, Louisiana State University, Baton Rouge, USA 70803

[†] Equal contribution

* Correspondence: mgartia@lsu.edu; carges@lsu.edu

Abstract

Electrochemical properties of most supercapacitor devices degrade quickly when the operating temperature deviates from room temperature. In order to exploit the potential of rGO in supercapacitors at extreme temperatures, a resilient electrolyte that is functional over a wide-temperature range is also required. In this study, we have implemented a flexible, low-resistant solid-state electrolyte membrane (SSEM) into symmetric rGO electrodes to realize supercapacitor devices that operate in the temperature range of -70 °C to 220 °C. The SSEM consists of a polycation-polybenzimidazole blend that is doped with phosphoric acid (H₃PO₄) and this material displays uniquely high conductivity values that range from 50 mS cm⁻¹ to 278 mS cm⁻¹ in the temperature range of -25 °C to 220 °C. The fabricated supercapacitor produced a maximum capacitance of 6.8 mF cm⁻² at 100 °C. Energy and power densities ranged from 0.83 to 2.79 mW h cm⁻² and 90 to 125 mW cm⁻², respectively. The energy storage mechanism with a SSEM occurs by excess H₃PO₄ migrating from the membrane host into the electrochemical double layer in rGO electrodes. The high temperature operation is enabled by the polycation in the SSEM anchoring phosphate type of anions preventing H₃PO₄ evaporation. Low temperature operation of the supercapacitor with the SSEM is attributed to the PC-PBI matrix depressing the freezing point of H₃PO₄ to maintain structural proton diffusion.

Keywords: Supercapacitor; Flexible; Reduced Graphene Oxide; Solid-State Electrolyte Membrane; High and Low Temperature; Energy Storage

1. Introduction

Supercapacitors are well-known for low equivalent internal series resistance, high cycling stability as well as providing high power density.¹⁻³ These properties are responsible for the ever-increasing interest in supercapacitors for a wide-range of energy storage purposes (e.g., biomedical devices, starting electric vehicles, etc.).⁴ To increase the utility of these devices for consumer and aerospace applications, there is a need for producing supercapacitors with lower form factor and that operate over a wide temperature range. Introducing graphene-based supercapacitors redefined their applications by producing flexible, thin and light energy storage devices that can fit into various multifunctional electronics.⁵⁻⁶ However, most supercapacitor and batteries technologies operate in a narrow temperature range and are not suited for both low and high temperature operation.⁷ The temperature limitation for supercapacitor is primarily related to the electrochemical properties of materials, which are a strong function of temperature.⁸⁻¹⁰ As a result of the materials limitation, most of the reported literature on supercapacitors only report device operation at room temperature. Hence, there are very few studies that report supercapacitor devices that operate at both high and low temperatures.¹¹⁻¹³ Furthermore, only a small subset of these studies showed cycling properties of these devices at extreme temperatures because the device performance measurements at the temperature extremes is challenging.¹³

In order to realize a supercapacitor technology tolerant of extreme temperatures, it is paramount to select functional materials under the temperature range desired. The major components that makeup a supercapacitor consists of an electrolyte, electrodes, current collectors, and packaging. Among these, electrode and electrolyte functionality have limited temperature range and thus are the main limiting factors for enabling supercapacitor technology that performs over a wide-temperature range.¹⁴⁻¹⁵ Despite some attempts to increase the operating temperature range of electrode materials, working temperature of activated carbon and onion-like carbon is still constrained to -10 to 100 °C and -50 to 80 °C, respectively.¹⁶⁻¹⁸ Reduced graphene oxide (rGO) electrodes, on the other hand, provide functionality in the temperature range (-40 to 200 °C) for supercapacitor applications.¹³ Hence, rGO is a suitable electrode material for fabricating a wide-

temperature range supercapacitor, but a robust electrolyte that is functional at both extremely low and high temperatures has been elusive.

Supercapacitor electrolytes are usually categorized into liquid electrolytes (ionic, organic and aqueous liquids) and solid-state electrolytes (mainly polymer or particle gels). Solid-state electrolytes potentially perform better at both extremely high temperatures ($> 100\text{ }^{\circ}\text{C}$) and low temperatures ($< 0\text{ }^{\circ}\text{C}$).¹⁹ Additionally, solid-state electrolytes offer the prospect to mitigate problems associated with liquid electrolytes such as shunt currents and fire hazards. Plus, they enable a thinner and flexible design.²⁰ However, the main limitation of using solid-state electrolytes relates to their lower conductivity (100 to 1000 times lower) compared to liquid electrolytes.²¹⁻²² Therefore, overcoming the ionic conductivity hurdles of solid-state electrolytes is needed to realize supercapacitors that operate effectively over a wide temperature range.

Most solid-state electrolytes for supercapacitors utilize a polymer or particle gel host. The viscous nature of these materials hinders device flexibility and do not provide good ionic conductivity. A less explored option as a solid-state electrolyte for supercapacitor devices are ion-exchange membranes (e.g., proton exchange membranes (PEMs) and anion/hydroxide exchange membranes (AEMs)).²³⁻²⁴ PEMs and AEMs have been deployed in various electrochemical processes, such as fuel cells,^{23, 25} but these membrane variants for these applications do not traditionally contain any excess electrolyte that can flow in and out of the membrane making them undesirable for supercapacitor applications. Furthermore, their ability to provide ionic conduction is strongly correlated to high levels of hydration for counterion ion dissociation from tethered ionic groups to the polymer backbones.^{23, 25} Enabling anhydrous proton conduction in PEMs for fuel cells that operate in the temperature range of 120 to 180 $^{\circ}\text{C}$ was achieved over 25 years using phosphoric acid (H_3PO_4) doped PBI.²⁶ These PEMs, H_3PO_4 -PBI, has been implemented in solid-state, high temperature (25 to 150 $^{\circ}\text{C}$) supercapacitors,^{14, 27-30} but they have not been evaluated at temperatures below 25 $^{\circ}\text{C}$ (even frigid temperatures of less than 0 $^{\circ}\text{C}$) and their performance cannot be evaluated above 180 $^{\circ}\text{C}$ as the H_3PO_4 starts to evaporate from PBI.³¹⁻³³ Our group has recently extended the temperature range of anhydrous PEMs through the use of polycation-PBI polymer blend doped with H_3PO_4 .³⁴ The polycation in the blend was Udel[®] poly (arylene ether sulfone) featuring quaternary benzyl pyridinium cations (QPPSf). The H_3PO_4 -QPPSf-PBI showed remarkably high in-plane proton conductivity (up to 290 mS cm^{-1} at 220 $^{\circ}\text{C}$) and excellent

mechanical properties (11.9 MPa at break and 25% elongation), while also endowing long-term thermal stability at 220 °C and stability in the presence of water vapor.³⁴ In this work, we not only show that the solid-state electrolyte membrane (SSEM) of H₃PO₄-QPPSf-PBI blend can extend the temperature range to 220 °C for an all solid-state, flexible supercapacitor with rGO electrodes, but this SSEM also fosters proton conduction as low as -70 °C. Therefore, the polycation-PBI SSEM incorporated with rGO electrodes has resulted in a supercapacitor technology for applications necessitating a wide temperature range.

2. Materials and Methods

2.1. Preparation of Solid-State Electrolyte

Chloromethylated poly(arylene ether sulfone) (CMPSf) was prepared via a Friedel-Crafts reaction following the procedure reported by Arges *et al.*³⁵ An example reaction is as follows: 10 g of Udel[®] poly(arylene ether) sulfone (PSf) was dissolved in 500 ml of chloroform in a round bottom flask. Once the PSf dissolved, 6.8 g of paraformaldehyde followed by 30 mL of chlorotrimethylsilane was added. The bulb was sealed using rubber septum and filled with nitrogen. 525 µL of SnCl₄, the Lewis acid catalyst, was added to the sealed bulb. The degree of functionalization (DF) (i.e., chloromethyl groups per repeat unit) was monitored during the reaction by withdrawing a sample from the flask. The withdrawn solution was cooled to room temperature and precipitated in methanol (5:1 volume ratio of methanol to reaction solution). The precipitate was collected via vacuum filtration and dried and then analysed via ¹H NMR. When the desired DF values for the CMPSf was attained, the whole reaction solution was cooled to room temperature followed by precipitation in methanol (5:1 volume ratio). The precipitate was collected via vacuum filtration and air dried in the fume hood. The solid was redissolved in chloroform (5wt %) and then precipitated in methanol (5:1 volume ratio) to remove impurities. The solid was collected via vacuum filtration and then vacuum dried at room temperature. The DF value of the purified CMPSf was determined via ¹H NMR.

The preparation of the blended membrane was recently reported in our work.³⁴ A brief description of the method is given here: CMPSf was dissolved in N,N-dimethylacetamide (DMAc) to attain a 5 wt% solution. A similar 5 wt% solution of PBI in DMAc was prepared. Equal volume ratios of PBI and CMPSf solutions were mixed to prepare a solution blend. The mixed solutions

were sonicated for half an hour and then drop casted on a levelled glass plate in oven at 120 °C for 6 hours. The dried membranes were peeled off from the glass plates and were immersed in pyridine solution (1M in reagent alcohol) at 40 °C for 16 hours to convert the chloromethylated groups to quaternary benzyl pyridinium chloride groups. The resulting membranes were washed with DI water and blot dried. The thickness of the membranes ranged from 36-50 μm. The membranes were then immersed in 85 wt% phosphoric acid (H₃PO₄) at 120 °C for 6 hours. The membranes were then blot dried to remove the excess acid. The thermal stability, ion-exchange capacity, ¹H NMR of QPPSf, and mechanical properties of the membranes were reported in our previous work.³⁴

In-plane proton conductivity (κ_{H^+}) measurements were performed using galvanostatic impedance spectroscopy with a Gamry 3000 AE potentiostat over a frequency range of 1 MHz to 1 Hz using a 0.1 mA perturbation in a four-point conductivity probe (platinum wires and meshes in a PTFE housing). The κ_{H^+} (mS cm⁻¹) of the membranes were found using:

$$\kappa_{H^+} = \frac{L}{R \times D \times W} \quad (1)$$

where L (cm) is the distance between the electrodes, R (mΩ) is the resistance of the membrane, D (cm) is the thickness of the membrane and W (cm) is the width of the membrane. The κ_{H^+} was measured in a temperature-controlled oven (-70 to 220 °C). Three different thermal cycles performed for three individual membrane samples. During each cycle, the conductivity was measured from -70 to 220 °C at different points. The membranes were equilibrated at 25 °C before proceeding to the next cycle (-70 to 220 °C). Thermal gravimetric analysis (TGA) of undoped, H₃PO₄ doped QPPSf-PBI membranes and rGO electrodes were performed under nitrogen using Pyris 1 TGA (TA instruments). The samples were initially heated to 100 °C and equilibrated at that temperature for 10 minutes. Then, the samples' temperature was heated up to 700 °C at the rate of 10 °C min⁻¹. The phase transition in H₃PO₄ doped QPPSf-PBI membrane was recorded using DSC Q-10 (TA instruments) under nitrogen at heating rate of 10 °C min⁻¹ from 60 °C to -40 °C.

2.2. Preparation of rGO Electrodes

High quality water-dispersed graphene oxide (GO) was purchased from Graphenea Inc., Cambridge, MA with GO concentration of 4 mg mL⁻¹ and monolayer content of >95 %. For proper

exfoliation of the GO, water-dispersed GO was sonicated for 30 minutes in a sonication bath. Afterwards, the GO solution was drop-cast on the surface of a Teflon[®] sheet and dried at room temperature overnight. The reason for using Teflon[®] sheet is to prevent the adherence of reduced graphene oxide (rGO) to the temporary substrate. Neewer PRO i-TTL xenon camera flash was employed for reduction of GO to rGO under ambient conditions. Gentec QE25ELPS-MB-INT-D0 light energy meter was used to measure the energy of camera flash which was in the range of 0.1-2 J cm⁻². A small explosion sound was heard after flashing the GO and the produced rGO easily detached from the Teflon[®] surface afterwards. Color change from brown to black was indicated successful GO to rGO conversion. Sandwich type devices were made by packing the electrodes and membrane by means of temperature resistant Kapton[®] tape. Copper tape was used for collecting and passing charge from electrodes.

2.3. Electrochemical Tests on the Device

Electrochemical tests were performed on sandwich type devices made of rGO flash reduced electrodes and QPPSf-PBI electrolyte. GAMRY 1010E potentiostat was employed to perform the galvanostatic charge discharge (GCD), cyclic voltammetry (CV) and electrochemical impedance spectroscopy (EIS). Kryo 560-16 controlled rate freezer was used to cool down the temperature from 25 to -70 °C. VWR standard oven was employed to test the device at high temperatures (up to 220 °C). Before all the temperature dependent tests, the device was held at the desired temperature for 10 min to reach the temperature equilibrium. EIS experiments were performed in the range of 100 kHz to 1 Hz. From CV curves, areal capacitance was calculated from equation 2:

$$C_v = \frac{\int i \cdot dV}{v \cdot \Delta V \cdot v} \quad (2)$$

In which, ΔV is the potential window (V), i is the current (A) and v is the area of the active material (cm²). From GCD plots, areal capacitance was measured by using the following equation:

$$C_v = \frac{-idt}{v \Delta V} \quad (3)$$

In which, t is value of discharge time. Energy (E) and power (P) density values obtained by equation 4 and 5:

$$E = \frac{C_v \times (\Delta V)^2}{3600} \quad (4)$$

$$P = \frac{E \times 3600}{\Delta t} \quad (5)$$

2.4. Materials Characterization

Scanning electron microscope images were obtained by Quanta 3D DualBeam FEG FIBSEM with working distance of 10.2 mm and accelerating voltage of 5 kV. Fourier-transform infrared spectroscopy (FTIR) and Raman spectroscopy were performed by Thermo Nicolet Nexus 670 ATR-FTIR (total # of scans = 64) and Renishaw inVia confocal Raman microscope, respectively. Laser 532 nm was used for Raman spectroscopy of samples in the range of 500-3000 cm^{-1} and exposure time of 10 s.

3. Results and Discussion

Figure 1 illustrates the sandwich type device made by flash reduced rGO electrodes and the 50:50 H_3PO_4 -QPPSf-PBI. The inset of the **Figure 1** shows the chemical structure of the H_3PO_4 -QPPSf-PBI. This polycation-PBI blend for the SSEM was prepared using a process disseminated in our previous work (see **Figure S1**).³⁴ Briefly, the polycation, Udel[®] poly(arylene ether sulfone) with quaternary benzyl pyridinium, was synthesized by first performing Friedel-Crafts chloromethylation of commercially available Udel[®] poly(arylene ether sulfone).³⁶ The chloromethylated polymer dissolved in N,N-dimethylacetamide (DMAc, 5 wt%) was blended at a 50:50 ratio with commercially acquired PBI in DMAc (5 wt%, PBI Performance Products).³⁶ The blended polymer solutions were drop casted to prepare a free-standing membrane with thickness varying from 36 to 48 μm . The membrane was then immersed in 1 M pyridine (reagent alcohol solvent) to convert the chloromethyl groups to quaternary benzyl pyridinium chloride groups. The final step imbibed H_3PO_4 into the polymer matrix by soaking in 85 wt% $\text{H}_3\text{PO}_{4(\text{aq})}$ at 120 °C for 6 hours. In our previous work³⁴ varying blends of H_3PO_4 -QPPSf-PBI were prepared, and the 50:50 blend yielded the highest conductivity and best mechanical and thermal stability. Hence, the 50:50 H_3PO_4 -QPPSf-PBI blend was evaluated as a SSEM for supercapacitor device studies.

3.1. Materials Characterization of the Membrane and the Electrodes

Prior to device studies, Raman spectroscopy (**Figure 2a**) and ATR-FTIR (**Figure 2b**) identified the different chemical moieties in the H_3PO_4 -QPPSf-PBI membrane and the non-acid

doped QPPSf-PBI membrane. The peak at 1539 cm^{-1} in the Raman spectra in the non-acid doped SSEM was ascribed to the imidazole group present in PBI, while the peak at 1610 cm^{-1} corresponded to the C-N⁺ stretching in the pyridinium moiety. The FTIR peak at 2924 cm^{-1} was attributed to the methylene group that tethered the cation to the poly (arylene ether sulfone) backbone and the methyl groups in the iso-propyl moiety in the poly (arylene ether sulfone) backbone. The FTIR peak at 1487 cm^{-1} came from the C-H stretching the arylene rings and the pyridinium cation.³⁷⁻³⁸ After immersing the membrane in H₃PO₄, the peak at 1539 cm^{-1} in the Raman spectra shifted to 1570 cm^{-1} because the H₃PO₄ protonated the imidazole in PBI to yield imidazolium.³⁷⁻³⁸ A broad FTIR peak in the range $2400\text{-}3000\text{ cm}^{-1}$ for the acid-doped in the SSEM was ascribed to the N-H stretching in the protonated PBI. Furthermore, a significant vibration at 956 cm^{-1} in the FTIR was observed and was attributed to the P=O in H₃PO₄.³⁷⁻³⁸

Table S1 (see *Supporting Information*) reports the properties of the H₃PO₄-QPPSf-PBI SSEM.³⁴ The acid uptake of membrane was 220% and the ion-exchange capacity (IEC) of the non-acid doped SSEM (on a base group basis) was 4.1 mequiv g⁻¹. Normalizing the acid uptake to the IEC resulted in a H₃PO₄ level per base moiety (nH₃PO₄ B⁻¹) of 7.9. The H₃PO₄-QPPSf-PBI SSEM gave an ultimate tensile strength of 11.9 MPa at 25% elongation at break. The excellent toughness of the membrane, and its ability to be moderately stretched, made it a good candidate for electrochemical devices that need some degree of flexibility like wearable electronics.

The thermal stability of the acid-doped and undoped SSEM was assessed with thermogravimetric analysis (TGA). The TGA curves are presented in **Figure 2c**. The undoped membrane exhibited two stages of weight loss. The first region between $220\text{-}275\text{ }^{\circ}\text{C}$ was due to the degradation of the pyridinium group and the second weight loss region between $450\text{-}700\text{ }^{\circ}\text{C}$ derived from degradation of the polymer backbone. The H₃PO₄ doped membranes displayed an initial weight loss in the temperature range of $100\text{-}160\text{ }^{\circ}\text{C}$ and this was attributed to residual water evaporation. The second weight loss in the temperature range of $160\text{-}250\text{ }^{\circ}\text{C}$ was due to minor evaporation of H₃PO₄ and condensation of H₃PO₄ to triphosphoric acid, pyrophosphoric acid, or polyphosphoric acid and some quaternary benzyl pyridinium degradation.^{34, 39} The other weight loss regions observed from $300\text{-}700\text{ }^{\circ}\text{C}$ were ascribed to polymer backbone degradation. The interaction of phosphate anions with the pyridinium cations prevents the bulk of H₃PO₄ from evaporating between $160\text{-}250\text{ }^{\circ}\text{C}$ from the QPPSf-PBI polymer host.³⁴ With respect to stability,

the H₃PO₄-QPPSf-PBI SSEM retained 85% of its in-plane proton conductivity at 220 °C for 96 hours. This stability test showed the initial proton conductivity drop within 24 hours was due to excess acid evaporation followed by no changes in proton conductivity over the next 72 hours. The thermally stability data provided confidence that the H₃PO₄-QPPSf-PBI SSEM would be an effective electrolyte candidate for supercapacitor devices in the temperature range of 25-220 °C.

An important PEM property is its ability to foster adequate proton conductivity across a wide-temperature range. **Figure 2d** presents the proton conductivity of the H₃PO₄-QPPSf-PBI SSEM from -70 to 220 °C. For the temperature range between 25 to 220 °C, the proton conductivity increase was commensurate with rising temperature values. As the temperature increases, the structural diffusion of protons in the hydrogen bonded network becomes greater. Surprisingly, the H₃PO₄-QPPSf-PBI SSEM displayed higher conductivity at -20 °C versus 25 °C.³⁴ The ionic conductivity measurements were performed under ambient laboratory settings and it is known that residual water in H₃PO₄ disrupts the hydrogen bonded network hindering facile ionic conductivity.^{34, 40} Therefore, cooling the environment down to -20 °C reduced/eliminated the partial pressure of water in the environment and this resulted in an increase in the SSEM's proton conductivity when compared to the value at 25 °C. It is worth noting that pure H₃PO₄ is a solid at room temperature, but this acid imbibed into the polycation-PBI host depresses its freezing point enabling proton conductivity as high as 50 mS cm⁻¹ at -20 °C. Reducing the temperature from -20 to -70 °C severely compromises proton conductivity. The reduction in proton conductivity below -20 °C could be realized from the differential scanning calorimetry (DSC) for H₃PO₄ doped QPPSf-PBI (**Figure S2**). **Figure S2** shows two peaks, one at 0 °C and other at -15 °C. The former peak could be corroborated to the reduction in partial pressure of water in the environment, whereas the latter peak was observed due to complete immobilization of phosphate anion due to crystallization.

The proton conductivity at -70 °C is 0.01 mS cm⁻¹. Although this value is at least a 4-order magnitude reduction of the maximum proton conductivity observed, the value of 0.01 mS cm⁻¹ for conductivity still rivals some lithium salt containing polymer electrolytes for lithium ion batteries.⁴¹ It will be shown later on that the supercapacitor device can still operate at the extreme low temperature of -70 °C with the H₃PO₄-QPPSf-PBI SSEM despite the high ohmic penalty. Finally, it is important to note that this proton exchange membrane displayed repeatable

conductivity values (n=3 repeat traces plotted in **Figure 2d**) when evaluating the temperature across the range of -70 to 220 °C. During each cycle, the temperature was ramped up from room temperature to 220 °C and cooled to -70 °C and ramped up to 220 °C. Individual temperature points were held while performing EIS measurements. In-plane proton conductivity loss and stability of the membranes in the temperature range was assessed by performing cycling tests.

The data presented in **Figure 2d** and **Table S1** signify that the H₃PO₄-QPPSf-PBI SSEM offers excellent proton conductivity over a wide-temperature range (over 50 mS cm⁻¹ from -25 to 220 °C), while being thermally stable at the elevated temperature of 220 °C and mechanically robust. The molecular origins behind the exceptional conductivity of the H₃PO₄ doped polycation-PBI membrane was assigned to: i.) the cationic groups on the polycation promote greater hydrogen bonding frustration as they do not accept a proton like PBI and ii.) the presence of PBI in the blend allows for greater H₃PO₄ uptakes – which is not the case for most polycation membranes that are typically used in AEMs. Furthermore, the cations in the polycation create electrostatic interactions that are an order magnitude stronger with phosphate type anions over the acid-base interactions in H₃PO₄-PBI.³¹ Thus, the stronger electrostatic interactions can extend the upper temperature range of the membrane without concern of H₃PO₄ evaporation. Now that the proton exchange membrane can withstand temperatures greater than 180 °C (and up to 220 °C) by mitigating H₃PO₄ evaporation, the increased temperature value to 220 °C promotes structure proton diffusion and higher ionic conductivity. With regard to the below room temperature proton conductivity, there is no literature available on H₃PO₄ doped polycations and sparse reports on H₃PO₄-PBI. As previously stated, pure H₃PO₄ is a solid at room temperature. Mixing this acid with the polycation-PBI polymer host disrupts the hydrogen bonded network in H₃PO₄ preventing it from becoming a solid at low temperatures. With this effect, it is possible to maintain structure proton diffusion within the SSEM and proton conductivity at depressed temperatures.

With the properties H₃PO₄-QPPSf-PBI SSEM established, it is important to focus on the electrode properties used in the supercapacitor demonstrations across the wide-temperature range. **Figure 3a** provides a cross-sectional SEM image of flash reduced rGO. As showed in our previous work,⁴² graphene sheets are delaminated due to the camera flash reduction process. The color of the surface changed from brown to black indicating production of rGO from GO (**Figure S1**). By flashing the GO, oxygen atoms escape the layered structure of graphene oxide accompanied by

producing a small explosion sound. This micro-explosion increases the inter-layer distance between the produced multilayered graphene structures.⁴² As a result, the high surface area of rGO is activated and this is an important property for electrochemical charge storage. More details about reduction of graphene oxide via flash reduction method is explained elsewhere.⁴² **Figure 3b** shows the ATR-FTIR spectrum obtained from GO and rGO. A strong hydroxyl group stretching peak is observed at 3412 cm^{-1} for GO, but this signal is almost eliminated after flash reduction.⁴³ At 1713 cm^{-1} , C=O carbonyl stretching peak has a much higher intensity in GO compared to rGO.⁴⁴ The peak at 1020 cm^{-1} shows the existence of oxygen in the multilayered graphene structure.⁴³ As can be seen, the intensity of this peak decreases by $\sim 40\text{X}$ after the flash reduction of GO and thus provides further evidence for the successful conversion of GO to rGO via flash reduction method.

Raman spectra (**Figure 3c**) provided additional evidence of GO conversion to rGO using the flash reduction process. The doublet peak located at 2651 cm^{-1} corresponded to the existence of multilayered graphene and supported the reduction of GO to rGO. The G band in **Figure 3c** shifted slightly from 1585 to 1581 cm^{-1} after the flash reduction and this shift derives from the formation of a 3D structure by delamination of graphene layers and topological disordering.⁴⁵ I_D/I_G ratio has also changed from ~ 0.93 in GO to ~ 1.16 in rGO sample demonstrating the removal of oxygen species in the reduced sample.⁴⁵ Shifting of D^* band from 1563 cm^{-1} (for GO) to 1499 cm^{-1} (rGO) also showed a decrease in the amount of oxygen content after the flash reduction. The spectra in **Figures 3b** and **3c** unequivocally demonstrate the production of rGO electrodes from GO using the flash reduction method and the electron micrograph in **Figure 3a** demonstrates that the reduction process results in porous, layered electrodes.

3.2. Room-Temperature Electrochemical Tests

Figure 4a is a picture of an assembled all-solid-state and flexible supercapacitor with rGO as working electrodes and H_3PO_4 -QPPSf-PBI SSEM. The measured current and capacitance values from all device electrochemical experiments were normalized to the geometric area of the device. **Figure 4b** shows the CV curve of rGO-50:50 H_3PO_4 -QPPSf-PBI SSEM at 10, 50, 100 and 1000 mV s^{-1} scan rates at room temperature (20 to $22\text{ }^\circ\text{C}$). Inspection of the CV curves reveals the formation of a double-layer capacitance because the traces are symmetric in shape and are largely rectangular across the potential range. We assert that excess H_3PO_4 in the polymer host is responsible for ions that can be stored in the electrochemical double layer (EDL) of rGO

electrodes. There was no imbibing of acid into the electrodes during fabrication of the capacitor device. Hence, the only source of ions that could be adsorbed in the EDL hailed from the SSE membrane. Our previous research³⁴ has showed that not all of the imbibed acid in the polymer blend membrane is anchored through electrostatic interactions and some of the excess acid can leach out of the membrane. As observed with most electrochemical capacitors featuring carbon electrodes, increasing the scan rate results in larger current response and a bigger rectangular area. For example, $400 \mu\text{A cm}^{-2}$ was produced at a scan rate of 10 mV s^{-1} and $3900 \mu\text{A cm}^{-2}$ was generated at a scan rate 1000 mV s^{-1} . The value of areal capacitance was determined at a current density of 1 mA cm^{-2} from the galvanostatic charge-discharge (GCD) plot (**Figure 4c**) and found to be 3 mF cm^{-2} at room temperature. The symmetric and linear shape of GCD curve also shows the double layer capacitance nature of the device. The slight deviations from the perfect double layer capacitance shape in CV and GCD curves may originate from inevitable impurities of the system (residual oxygen) and surface reactions (redox reactions due to residual oxygen). The energy density and power density values of the supercapacitor at room temperature ranged from $0.83\text{-}2.79 \text{ mW h cm}^{-2}$ and $90\text{-}125 \text{ mW cm}^{-2}$, respectively. Because a mechanically robust SSEM was adopted, the supercapacitor device could be bent up to 180° while retaining its original CV shape (**Figure 4d**). These results confirm the outstanding electrochemical properties of this all-solid-state device which is also fully flexible.

3.3. Extreme-Temperature Electrochemical Tests

After analyzing the general electrochemical properties of the supercapacitor at ambient conditions, electrochemical properties of supercapacitor were measured across a wide temperature range. **Figure 5a** shows the CV plot of supercapacitor at scan rate of 50 mV s^{-1} in the temperature range of -70°C to 25°C . The inset for **Figure 5a** highlights that the device still operated at -70°C . The current density attained by the device continued to drop when cooling the capacitor from 25°C to -70°C . **Figure 5b** presents the CV curves of the supercapacitor device in the elevated temperature range of 25 to 220°C . The CV traces in both **Figures 5a** and **5b** were fairly symmetrical when operated across the voltage range of 0 to 1 V . The current response of the supercapacitor with the SSEM continued to increase when ramping the temperature from 25°C to 160°C . The CV curve at 100°C and 160°C were almost similar. Increasing the temperature beyond 160°C resulted in smaller current responses at 200°C and 220°C . The resultant device

capacitance values from the CV curves in **Figures 5a** and **5b** were plotted as a function of temperature in **Figure 5c**. There are two key takeaways from **Figure 5c**: i.) the maximum capacitance was observed at 100 °C and the value at 160 °C was pretty close to the value at 100 °C and ii.) the supercapacitor's capacitance value was on the same order of magnitude across the temperature range of -20 °C to 220 °C. Cooling the capacitor below -20 °C still resulted in a device that still operated but with a capacitance value that was about two orders in magnitude smaller. Despite the reduction of capacitance value below -20 °C, it is still higher than the recently published works for solid-state supercapacitors at low temperatures.^{11, 46}

To better understand why the supercapacitor displayed the highest capacitance at 100 °C and 160 °C and a dramatic reduction in capacitance at temperatures below -20 °C, electrochemical impedance spectroscopy (EIS) was performed to delineate the ohmic and diffusion resistance of ions in the electrodes as function of temperature. **Figure 6a-c** show the EIS of the supercapacitor with a SSEM at different temperatures. The Nyquist plots exhibited linear tails starting over the entire frequency range illustrating a diffusion-controlled mechanism for charge storage in the temperature range of -40 to 220 °C. The high frequency resistance (HFR) and the diffusion resistance were extracted from the Nyquist plots by fitting an electric circuit equivalent model to the data. The HFR occurred at where the Nyquist trace cross the x-axis. The diffusion resistance was determined from the slope of the real resistance (Z') versus reciprocal of the square root of frequency ($\omega^{-0.5}$) in the linear regime of the Nyquist plot (**Figure 6d, e and Figure S3**). **Figure 6f** plots the HFR and diffusion resistances as a function of temperature. The higher capacitance values that were commensurate with increasing temperature from 25 °C to 100 °C originated from improved structural proton diffusion in the SSEM that ultimately enhanced the conductivity of the SSEM leading to a lower HFR value. Plus, the improved conductivity also reduced the diffusion resistance of H₃PO₄ in the rGO electrodes. Between the temperature ranges of 100 °C to 160 °C, the diffusion resistance started to increase in **Figure 6f**. At 180 °C, the HFR also started to increase when increasing the temperature to 220 °C. The larger individual resistance values accounted for the decrease in capacitance observed above temperatures of 160 °C. At elevated temperatures, the migrated excess H₃PO₄ to the rGO electrodes may start to evaporate as there are no cationic groups to anchor them to the electrode – unlike the SSEM.^{31, 34} Furthermore, a fraction of the phosphoric acid undergoes dehydration at temperatures above 160 °C forming triphosphoric, pyrophosphoric, or polyphosphoric acid. These bigger acids may cause a small drop in SSEM ionic conductivity

and as a result a higher HFR value. Plus, these bigger acids cannot migrate as easy from the SSEM host into the rGO electrodes resulting in a larger diffusion resistance.

At temperatures below $-40\text{ }^{\circ}\text{C}$, a drastic increase in the HFR and diffusion resistance is observed (Figure 6). Since the proton conductivity is inversely proportional to the HFR, we will expect less available ions for the double layer formation. Therefore, the increase in resistances at low temperature conditions are leading to much lower capacitance values (i.e., below 1 mF cm^{-2}) compared to higher temperatures. Another reason for the rapid rise of diffusion resistance is attributed to the freezing of the H_3PO_4 in the polymer host restricting structural H_3PO_4 diffusion (as pointed out in Figure 2d and S2). Interestingly, semi-circles appeared in the Nyquist plot at $-50\text{ }^{\circ}\text{C}$, $-60\text{ }^{\circ}\text{C}$ and $-70\text{ }^{\circ}\text{C}$. These semi-circles indicated that a charge-transfer resistance may be occurring at these low temperatures. The origin of the apparent charge-transfer elements, which can be represented by a capacitor and a constant phase element in parallel, is currently unknown and will be the focus of future investigations. If the semi-circles are related to an electron-charge transfer process, such as corrosion of the electrodes or oxidation/reduction of oxygen, electrolyte, or water, it is unclear at the moment why this process would occur at -50 to $-70\text{ }^{\circ}\text{C}$ and not at greater temperatures. One possibility to explain the observation beyond a formal charge-transfer process may be related to the freezing of the electrolyte causing a poor interface between the electrode-electrolyte. This poor interface may be abrupt and could potentially be explained by a resistor and constant phase element in parallel. The molecular behavior of supercapacitors as such low temperatures is relatively un-explored and will be investigated in greater detail in the future.

Figure 7a presents the cycling stability of the device at $220\text{ }^{\circ}\text{C}$, $25\text{ }^{\circ}\text{C}$, and $-70\text{ }^{\circ}\text{C}$. The supercapacitor device retains 92% of its initial capacitance at room temperature after 5000 cycles. Inspection of reports in the peer-reviewed literature revealed that most high and low temperature supercapacitor studies do not perform cycling assessments at extreme temperatures. Surprisingly, the supercapacitor device maintained 81.5% of its capacitance at $-70\text{ }^{\circ}\text{C}$ after 5000 cycles. The device also retained more than 91% of its capacitance after 1000 cycles at $220\text{ }^{\circ}\text{C}$. However, capacitance retention reduced to 61% after 5000 cycles at the same temperature. The conversion of H_3PO_4 to polyphosphoric acids at $220\text{ }^{\circ}\text{C}$ may be responsible for the capacity of the fading over time. Overall, the SSEM capacitance device with rGO electrodes displayed better than expected

cycling stability and future efforts are underway to improve device performance and cycling retention.

In another stability assessment (**Figure 7b**), the supercapacitor device was held for 1 hour at individual temperatures in the temperature range of -70 to 220 °C and the GCD was measured after the 1-hour exposure, at room temperature. The curves in **Figure 7b** convey symmetrical shapes of the GCD curves after the temperature hold confirming device stability for at least 1 hour at the various temperatures. Comparison of the GCD diagrams at the different temperatures showed better stability of the supercapacitor devices at low temperatures (≤ 0 °C) than higher ones (≥ 100 °C). These results complement the cycling stability data generated in Figure 7a. It is noteworthy to mention that the specific capacitance of the device obtained by GCD curves after holding the device at different temperatures showed almost the same values (~ 3 mF cm⁻²).

Figure 8a reports capacitance retention of the device as a function of discharge current density in the range of 1 to 100 mA cm⁻². Charge storage in supercapacitors occurs by the formation of double layer capacitance at the interface of electrode and electrolyte. The electrochemical double layer is formed by diffusion of ions from electrolyte to the interface of electrode/electrolyte. It is crucial to examine the charge storage properties of the device at different temperatures. To this end, capacitance retention of the device at different temperatures was obtained by applying current densities in the range of 1 to 100 mA cm⁻² (**Figure 8a**). By deviating from room temperature and increasing the applied current density, specific capacitance of the device decreases. This difference is negligible at lower current densities. However, it becomes more evident at higher current densities due to ohmic losses. Accordingly, diffusion of the ions from electrolyte to electrode/electrolyte interface is limited at very high or low temperatures because at high temperatures polyphosphoric acids do not migrate well and at low temperatures the acid electrolyte is mostly a solid. **Figure 8b** shows the increase in working potential window of the device from 1 to 3.5 V by decreasing the temperature from 25 to -70 C. This can be explained by suppressing the occurrence of possible Faradaic reactions at high potentials by lowering the temperature. Faradaic reactions are restricted both thermodynamically and kinetically at extremely low temperatures. The occurrence of these Faradaic reactions mainly originates from redox reactions occurring due to the residual oxygen in the system. In our previous work,⁴² we have

shown the existence of residual oxygen in rGO electrodes which is mainly responsible for undesirable redox reactions.

Overall, the supercapacitor device developed herein with H₃PO₄-QPPSf-PBI SEM and rGO electrodes displayed energy storage capability across a large temperature range (-70 °C to 220 °C). In fact, to the best of our knowledge, this is widest temperature range a supercapacitor device. **Figure 8c** compares the areal capacitance vs. operating temperature range of our device and other similar recently published works. Accordingly, the supercapacitor with the SSEM in this work shows competitive areal capacitance and the largest temperature operation range compared to ionic liquid (IL) electrolytes and polyampholyte hydrogels,^{11, 46} Although the areal capacitance for polyvinyl alcohol (PVA) gel based electrolytes^{17, 47} is higher than what is reported in this work, the operating temperature of a supercapacitor with a polyvinyl alcohol (PVA) gel based electrolytes is limited to the temperature range of -40 to 60 °C. Additionally, H₃PO₄ doped PBI electrolyte only operates from room temperature to 160 °C.¹⁴ The wide operating temperature range of our device makes it possible to tolerate harsh environmental conditions in the range of -70 to 220 °C. Furthermore, a radar plot (**Figure S4**) summarizes all the different electrochemical properties of this device at a glance. The ability of the device to operate over a wide-temperature range is necessary for numerous applications that vary from wearable electronics to transportation and aerospace.

4. Conclusions

In this work, a solid-state and flexible supercapacitor was realized for extreme temperature applications by means of a novel polymer blend membrane and flash reduced graphene oxide electrodes. Raman and FTIR studies confirmed the formation of rGO from GO and revealed the various chemical species of the membrane. H₃PO₄ imbibed QPPSf-PBI blended membranes showed impressively high conductivity of 278 mS cm⁻¹ at 220 °C. Outstanding performance and thermal resistance of the device was confirmed by several electrochemical tests over a wide temperature range of -70 to 220 °C. Our device showed maximum capacitance of 6800 mF cm⁻³ at 100 °C. Energy density and power density were measured to be in the range of 0.83 to 2.79 mWh cm⁻² and 90 to 125 mW cm⁻², respectively. Formation of double layer capacitance was observed at both extremely low (-70 °C) and high (220 °C) temperatures. Working potential window of the device increased from 1 to 3.5 V by decreasing the temperature from 25 to -70 °C. This device

maintained 92% of its initial capacitance at room temperature after 5000 cycles. Furthermore, 81.5% of initial capacitance was preserved at -70 °C after 5000 cycles as well as 91% of its capacitance after 1000 cycles at 220 °C. Additionally, our supercapacitor demonstrated excellent flexibility by retaining its original CV curve shape after being bent up to 180°. As a result, the fully solid-state and flexible supercapacitor successfully operates in the temperature range of -70 to 220 °C as well as outperforming most of the current state of art solid-state supercapacitors at room temperature. Merging the aforementioned properties reveals new horizons for extreme temperature supercapacitors for challenging energy storage applications such as in aerospace, transportation and micro-electronics.

Supporting Information

Physical and mechanical properties of H₃PO₄ doped QPPSf-PBI; Synthesis and fabrication methods of membrane, rGO and the supercapacitor; DSC of H₃PO₄-QPPSf-PBI; The calculated slope values from the Z' vs. square root of frequency; Nyquist plots from EIS at -50 to -70 °C; Radar plot that shows different electrochemical properties of the supercapacitor device

Acknowledgements

M.R.G. acknowledges the support from LSU start-up fund, and Louisiana Board of Regents Support Fund (RCS Award Contract Number: LEQSF(2017-20)-RD-A-04). A.C. is supported by an LSU Economic Development Assistantship (EDA) grant. C.G. Arges acknowledges financial support for this work from LSU Lift², Louisiana Board of Regents (Proof-of-Concept/Prototype Initiative), 3M Non-Tenured Faculty Award, and start-up funds provided by the Cain Department of Chemical Engineering at LSU. We thank LSU Shared Instrumentation Facility and assistance provided by Dr. Dongmei Cao and Dr. Rafael Cueto.

References

1. Raza, W.; Ali, F.; Raza, N.; Luo, Y.; Kim, K.-H.; Yang, J.; Kumar, S.; Mehmood, A.; Kwon, E. E., Recent advancements in supercapacitor technology. *Nano Energy* **2018**, *52*, 441-473.
2. Kumar, K. S.; Choudhary, N.; Jung, Y.; Thomas, J., Recent advances in two-dimensional nanomaterials for supercapacitor electrode applications. *ACS Energy Letters* **2018**, *3* (2), 482-495.
3. Strauss, V.; Marsh, K.; Kowal, M. D.; El-Kady, M.; Kaner, R. B., A simple route to porous graphene from carbon nanodots for supercapacitor applications. *Advanced Materials* **2018**, *30* (8), 1704449.

4. Chen, C. R.; Qin, H.; Cong, H. P.; Yu, S. H., A Highly Stretchable and Real-Time Healable Supercapacitor. *Advanced Materials* **2019**, *31* (19), 1900573.
5. Meng, Y.; Zhao, Y.; Hu, C.; Cheng, H.; Hu, Y.; Zhang, Z.; Shi, G.; Qu, L., All-graphene core-sheath microfibers for all-solid-state, stretchable fibriform supercapacitors and wearable electronic textiles. *Advanced materials* **2013**, *25* (16), 2326-2331.
6. Xie, Y.; Liu, Y.; Zhao, Y.; Tsang, Y. H.; Lau, S. P.; Huang, H.; Chai, Y., Stretchable all-solid-state supercapacitor with wavy shaped polyaniline/graphene electrode. *Journal of Materials Chemistry A* **2014**, *2* (24), 9142-9149.
7. Xu, J.; Yuan, N.; Razal, J. M.; Zheng, Y.; Zhou, X.; Ding, J.; Cho, K.; Ge, S.; Zhang, R.; Gogotsi, Y., Temperature-independent capacitance of carbon-based supercapacitor from -100 to 60° C. *Energy Storage Materials* **2019**, *22*, 323-329.
8. Asbani, B.; Douard, C.; Brousse, T.; Le Bideau, J., High temperature solid-state supercapacitor designed with ionogel electrolyte. *Energy Storage Materials* **2019**, *21*, 439-445.
9. Yang, Y.; Ng, S. W.; Chen, D.; Chang, J.; Wang, D.; Shang, J.; Huang, Q.; Deng, Y.; Zheng, Z., Freestanding Lamellar Porous Carbon Stacks for Low-Temperature-Foldable Supercapacitors. *Small* **2019**, 1902071.
10. Masarapu, C.; Zeng, H. F.; Hung, K. H.; Wei, B., Effect of temperature on the capacitance of carbon nanotube supercapacitors. *ACS nano* **2009**, *3* (8), 2199-2206.
11. Newell, R.; Faure-Vincent, J.; Iliev, B.; Schubert, T.; Aradilla, D., A new high performance ionic liquid mixture electrolyte for large temperature range supercapacitor applications (-70° C to 80° C) operating at 3.5 V cell voltage. *Electrochimica Acta* **2018**, *267*, 15-19.
12. Vellacheri, R.; Al-Haddad, A.; Zhao, H.; Wang, W.; Wang, C.; Lei, Y., High performance supercapacitor for efficient energy storage under extreme environmental temperatures. *Nano Energy* **2014**, *8*, 231-237.
13. Zang, X.; Zhang, R.; Zhen, Z.; Lai, W.; Yang, C.; Kang, F.; Zhu, H., Flexible, temperature-tolerant supercapacitor based on hybrid carbon film electrodes. *Nano Energy* **2017**, *40*, 224-232.
14. Kim, S.-K.; Kim, H. J.; Lee, J.-C.; Braun, P. V.; Park, H. S., Extremely durable, flexible supercapacitors with greatly improved performance at high temperatures. *ACS nano* **2015**, *9* (8), 8569-8577.
15. Zequine, C.; Ranaweera, C.; Wang, Z.; Singh, S.; Tripathi, P.; Srivastava, O.; Gupta, B. K.; Ramasamy, K.; Kahol, P.; Dvornic, P., High performance and flexible supercapacitors based on carbonized bamboo fibers for wide temperature applications. *Scientific reports* **2016**, *6*, 31704.
16. Zeiger, M.; Jäckel, N.; Mochalin, V. N.; Presser, V., carbon onions for electrochemical energy storage. *Journal of Materials Chemistry A* **2016**, *4* (9), 3172-3196.
17. Nègre, L.; Daffos, B.; Turq, V.; Taberna, P.-L.; Simon, P., Ionogel-based solid-state supercapacitor operating over a wide range of temperature. *Electrochimica Acta* **2016**, *206*, 490-495.
18. Zhang, L. L.; Zhao, X., Carbon-based materials as supercapacitor electrodes. *Chemical Society Reviews* **2009**, *38* (9), 2520-2531.
19. Lv, T.; Liu, M.; Zhu, D.; Gan, L.; Chen, T., Nanocarbon-Based Materials for Flexible All-Solid-State Supercapacitors. *Advanced Materials* **2018**, *30* (17), 1705489.
20. Niu, Z.; Zhou, W.; Chen, X.; Chen, J.; Xie, S., Highly Compressible and All-Solid-State Supercapacitors Based on Nanostructured Composite Sponge. *Advanced materials* **2015**, *27* (39), 6002-6008.
21. Zhu, C.; Yang, P.; Chao, D.; Wang, X.; Zhang, X.; Chen, S.; Tay, B. K.; Huang, H.; Zhang, H.; Mai, W., All metal nitrides solid-state asymmetric supercapacitors. *Advanced Materials* **2015**, *27* (31), 4566-4571.
22. Tiruye, G. A.; Muñoz-Torrero, D.; Palma, J.; Anderson, M.; Marcilla, R., Performance of solid state supercapacitors based on polymer electrolytes containing different ionic liquids. *Journal of Power Sources* **2016**, *326*, 560-568.
23. Arges, C. G.; Zhang, L., Anion exchange membranes' evolution toward high hydroxide ion conductivity and alkaline resiliency. *ACS Applied Energy Materials* **2018**, *1* (7), 2991-3012.

24. Rosli, R.; Sulong, A. B.; Daud, W. R. W.; Zulkifley, M. A.; Husaini, T.; Rosli, M. I.; Majlan, E.; Haque, M., A review of high-temperature proton exchange membrane fuel cell (HT-PEMFC) system. *International Journal of Hydrogen Energy* **2017**, *42* (14), 9293-9314.
25. Kusoglu, A.; Weber, A. Z., New insights into perfluorinated sulfonic-acid ionomers. *Chemical reviews* **2017**, *117* (3), 987-1104.
26. Li, Q.; Jensen, J. O.; Savinell, R. F.; Bjerrum, N. J., High temperature proton exchange membranes based on polybenzimidazoles for fuel cells. *Progress in polymer science* **2009**, *34* (5), 449-477.
27. Soavi, F.; Bettini, L. G.; Piseri, P.; Milani, P.; Santoro, C.; Atanassov, P.; Arbizzani, C., Miniaturized supercapacitors: key materials and structures towards autonomous and sustainable devices and systems. *Journal of power sources* **2016**, *326*, 717-725.
28. Staiti, P.; Lufrano, F., Nafion® and Fumapem® polymer electrolytes for the development of advanced solid-state supercapacitors. *Electrochimica Acta* **2016**, *206*, 432-439.
29. Wei, Y.; Wang, M.; Xu, N.; Peng, L.; Mao, J.; Gong, Q.; Qiao, J., Alkaline Exchange Polymer Membrane Electrolyte for High Performance of All-Solid-State Electrochemical Devices. *ACS applied materials & interfaces* **2018**, *10* (35), 29593-29598.
30. Rathod, D.; Vijay, M.; Islam, N.; Kannan, R.; Kharul, U.; Kurungot, S.; Pillai, V., Design of an “all solid-state” supercapacitor based on phosphoric acid doped polybenzimidazole (PBI) electrolyte. *Journal of applied electrochemistry* **2009**, *39* (7), 1097-1103.
31. Lee, K.-S.; Spendelow, J. S.; Choe, Y.-K.; Fujimoto, C.; Kim, Y. S., An operationally flexible fuel cell based on quaternary ammonium-biphosphate ion pairs. *Nature energy* **2016**, *1* (9), 16120.
32. Lee, K.-S.; Maurya, S.; Kim, Y. S.; Kreller, C. R.; Wilson, M. S.; Larsen, D.; Elangovan, S. E.; Mukundan, R., Intermediate temperature fuel cells via an ion-pair coordinated polymer electrolyte. *Energy & Environmental Science* **2018**, *11* (4), 979-987.
33. Lee, A. S.; Choe, Y.-K.; Matanovic, I.; Kim, Y. S., The energetics of phosphoric acid interactions reveals a new acid loss mechanism. *Journal of Materials Chemistry A* **2019**, *7* (16), 9867-9876.
34. Venugopalan, G.; Chang, K.; Nijoka, J. D.; Livingston, S.; Geise, G. M.; Arges, C. G., Stable and highly conductive polycation-polybenzimidazole membrane blends for intermediate temperature polymer electrolyte membrane fuel cells. *ACS Applied Energy Materials* **2019**, *3* (1), 573-585.
35. Arges, C. G.; Parrondo, J.; Johnson, G.; Nadhan, A.; Ramani, V., Assessing the influence of different cation chemistries on ionic conductivity and alkaline stability of anion exchange membranes. *Journal of Materials Chemistry* **2012**, *22* (9), 3733-3744.
36. Palakkal, V. M.; Rubio, J. E.; Lin, Y. J.; Arges, C. G., Low-resistant ion-exchange membranes for energy efficient membrane capacitive deionization. *ACS Sustainable Chemistry & Engineering* **2018**, *6* (11), 13778-13786.
37. Deimede, V.; Voyiatzis, G.; Kallitsis, J.; Qingfeng, L.; Bjerrum, N., Miscibility behavior of polybenzimidazole/sulfonated polysulfone blends for use in fuel cell applications. *Macromolecules* **2000**, *33* (20), 7609-7617.
38. Zeis, R., Materials and characterization techniques for high-temperature polymer electrolyte membrane fuel cells. *Beilstein journal of nanotechnology* **2015**, *6* (1), 68-83.
39. Samms, S.; Wasmus, S.; Savinell, R., Thermal stability of proton conducting acid doped polybenzimidazole in simulated fuel cell environments. *Journal of the Electrochemical Society* **1996**, *143* (4), 1225-1232.
40. Schechter, A.; Savinell, R. F.; Wainright, J.; Ray, D., # 2# 1 and # 2# 1 NMR Study of Phosphoric Acid-Doped Polybenzimidazole under Controlled Water Activity. *Journal of the electrochemical society* **2009**, *156* (2), B283-B290.
41. Teran, A. A.; Tang, M. H.; Mullin, S. A.; Balsara, N. P., Effect of molecular weight on conductivity of polymer electrolytes. *Solid State Ionics* **2011**, *203* (1), 18-21.
42. Chaichi, A.; Wang, Y.; Gartia, M. R., Substrate Engineered Interconnected Graphene Electrodes with Ultrahigh Energy and Power Densities for Energy Storage Applications. *ACS applied materials & interfaces* **2018**, *10* (25), 21235-21245.

43. Sharma, N.; Sharma, V.; Jain, Y.; Kumari, M.; Gupta, R.; Sharma, S.; Sachdev, K. In *Synthesis and characterization of graphene oxide (GO) and reduced graphene oxide (rGO) for gas sensing application*, Macromolecular Symposia, Wiley Online Library: **2017**; p 1700006.
44. Ossoon, B. D.; Bélanger, D., Synthesis and characterization of sulfophenyl-functionalized reduced graphene oxide sheets. *RSC Advances* **2017**, 7 (44), 27224-27234.
45. Krishnamoorthy, K.; Veerapandian, M.; Mohan, R.; Kim, S.-J., Investigation of Raman and photoluminescence studies of reduced graphene oxide sheets. *Applied Physics A* **2012**, 106 (3), 501-506.
46. Li, X.; Liu, L.; Wang, X.; Ok, Y. S.; Elliott, J. A.; Chang, S. X.; Chung, H.-J., Flexible and self-healing aqueous supercapacitors for low temperature applications: polyampholyte gel electrolytes with biochar electrodes. *Scientific reports* **2017**, 7 (1), 1685.
47. Rong, Q.; Lei, W.; Huang, J.; Liu, M., Low Temperature Tolerant Organohydrogel Electrolytes for Flexible Solid-State Supercapacitors. *Advanced Energy Materials* **2018**, 8 (31), 1801967.

Figures

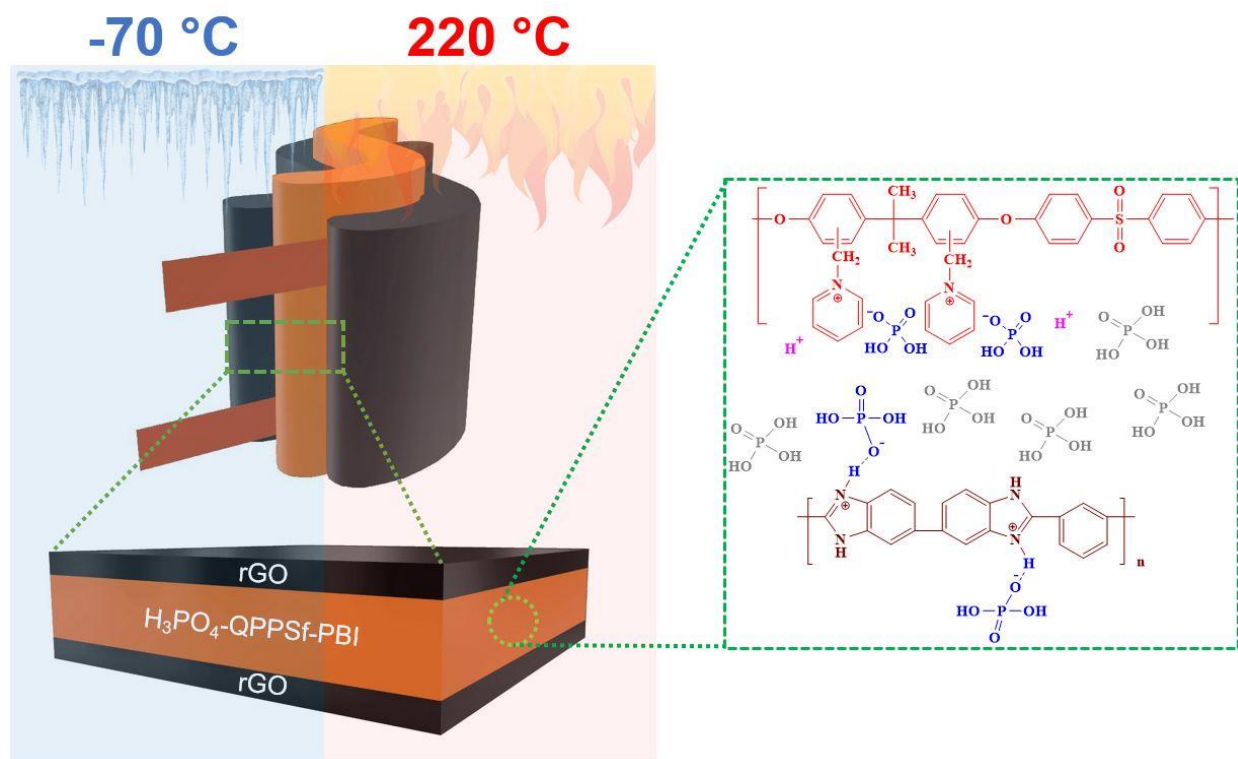


Figure 1. Schematic of the sandwich type supercapacitor design featuring rGO electrodes and H_3PO_4 -QPPSf-PBI based solid-state electrolyte membrane (SSEM). Chemical structure of the H_3PO_4 -QPPSf-PBI SSEM is given in the inset.

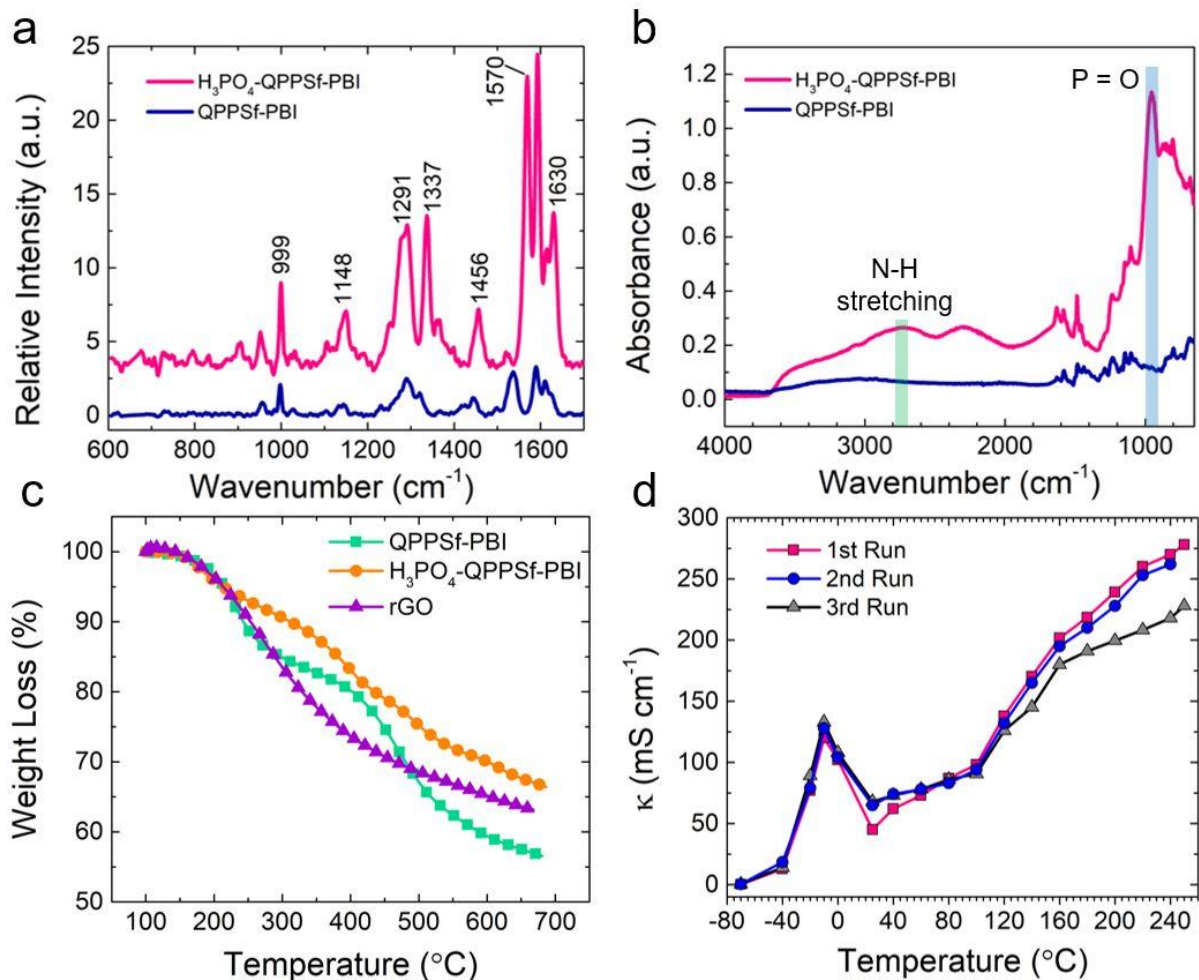


Figure 2. (a) Raman spectra of QPPSf-PBI with and without H_3PO_4 . (b) ATR-FTIR spectra of QPPSf-PBI with and without H_3PO_4 . Both Raman and FTIR spectra show the charged ionic moieties (e.g., pyridinium, imidazolium, and H_3PO_4) in the SSEM. (c) TGA curves for the pristine and H_3PO_4 imbibed QPPSf-PBI membranes and rGO electrode material. Each of these materials are thermally stable up to 220 $^{\circ}\text{C}$. (d) In-plane proton conductivity of the H_3PO_4 imbibed QPPSf-PBI membrane in the temperature range of -70 to 220 $^{\circ}\text{C}$.

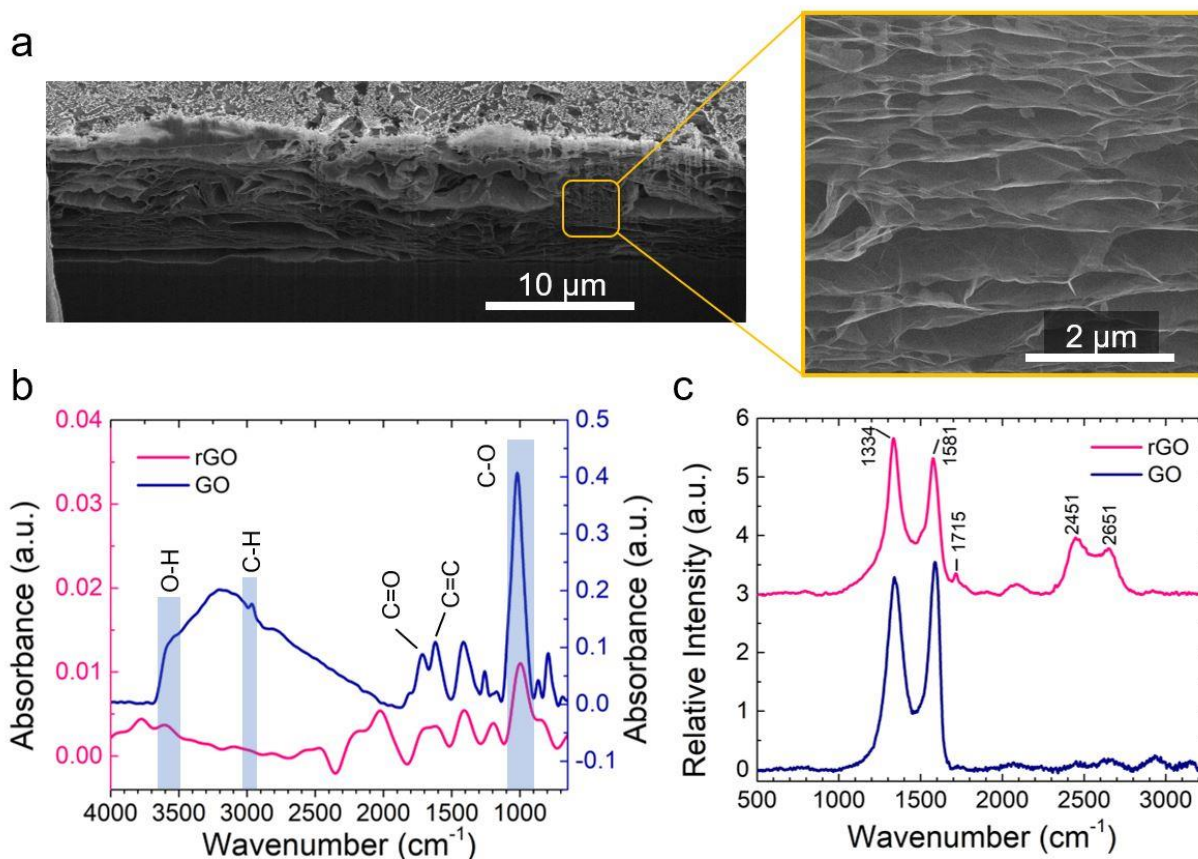


Figure 3. (a) Cross-sectional SEM image of rGO electrodes. The delaminated structure was observed after flash reduction of graphene oxide. (b) ATR-FTIR results of GO and rGO. The oxygen moieties were largely removed after reduction. Further, a peak at 1020 cm^{-1} confirmed the presence of multilayered graphene. (c) Raman spectra of GO and rGO and this spectroscopic technique also substantiated multilayered graphene as evident by the 2D peak at 2651 cm^{-1} .

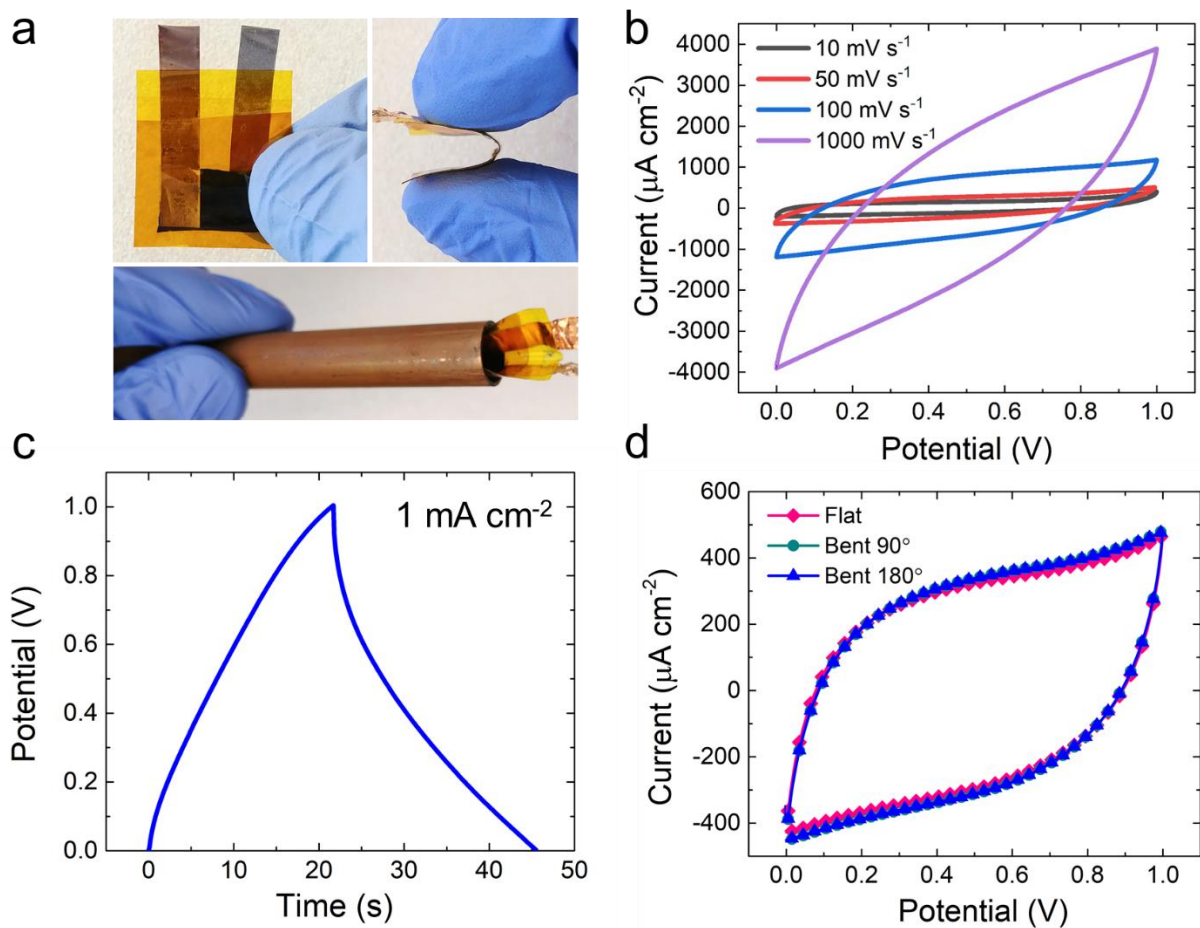


Figure 4. (a) Optical image showing the solid-state and flexible supercapacitor device made of rGO electrodes and H₃PO₄-QPPSf-PBI SSEM. (b) CV curve of the device obtained at 25 °C and at scan rates of 10, 50, 100 and 1000 mV s⁻¹. (c) Galvanostatic charge-discharge (GCD) plot at current density of 1 mA cm⁻². (d) Flexibility test of the supercapacitor devices (assessed by CV) performed at bending angles of 0° (flat), 90°, and 180°.

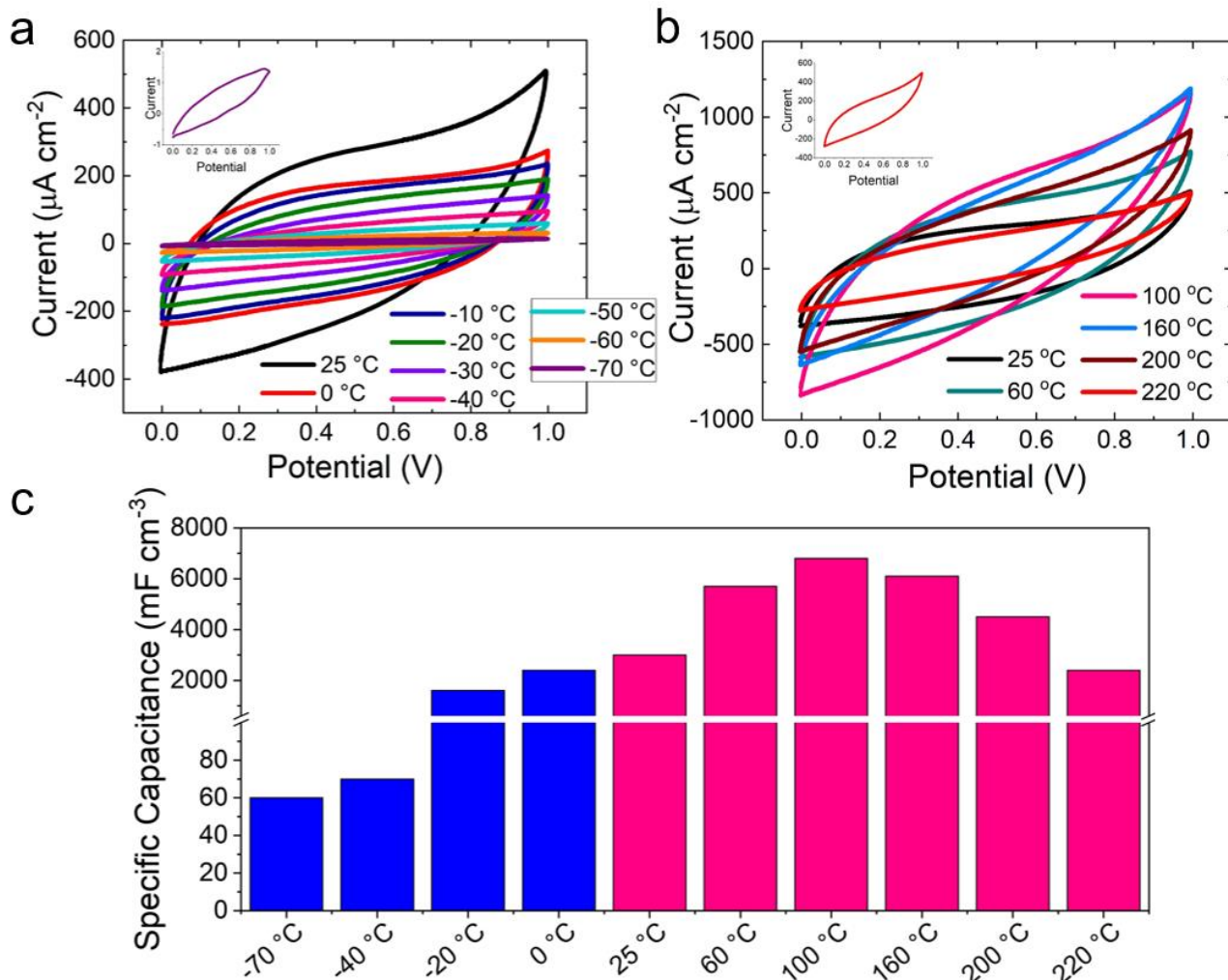


Figure 5. Electrochemical properties of the solid-state supercapacitor at different temperature values. (a) CV of supercapacitor at scan rate of 50 mV s^{-1} in the temperature range of -70 to $25\text{ }^{\circ}\text{C}$. (b) CV of supercapacitor in the range 25 to $220\text{ }^{\circ}\text{C}$. (c) The calculated values of specific capacitance determined from the CV plots at a scan rate of 50 mV s^{-1} . The maximum capacitance of the device was measured to be 6800 mF cm^{-3} and it was obtained at $100\text{ }^{\circ}\text{C}$.

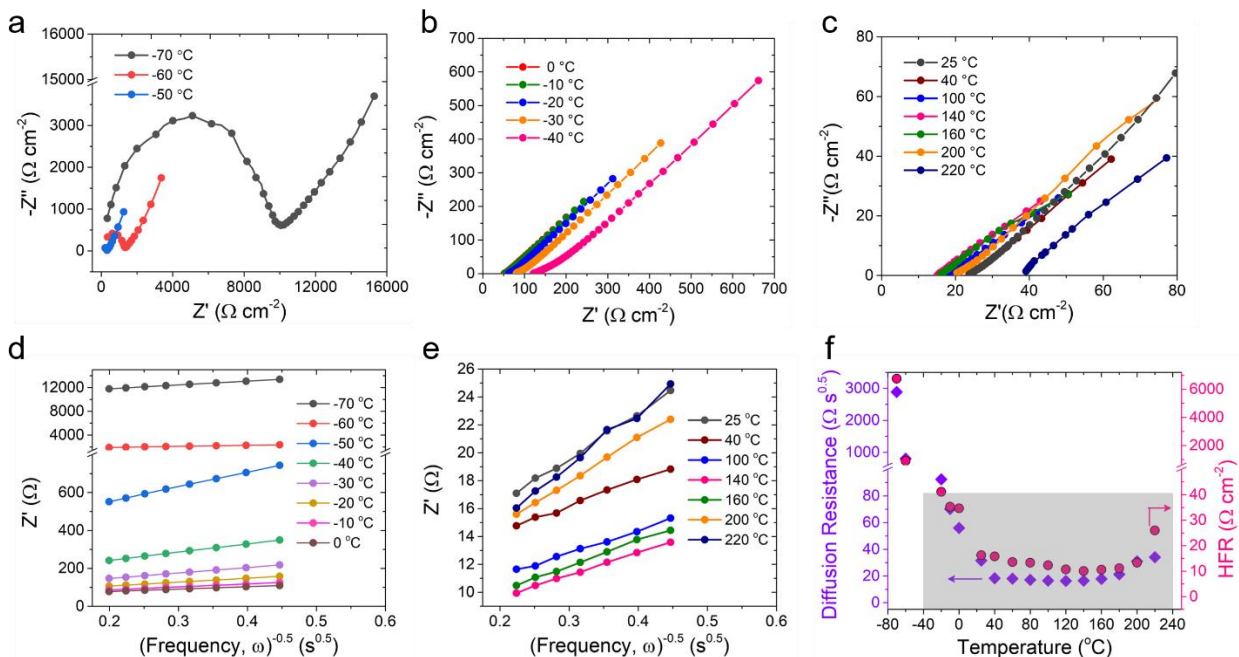


Figure 6. Nyquist plots from EIS experiment at (a, b) low to room temperature range (-70°C to 25°C), (c) high temperature range (40°C to 220°C). Z' vs. inverse square root of frequency from the EIS experiments to calculate the diffusion resistance is plotted at (d) low temperatures, and (e) high temperature ranges; (f) Diffusion resistance and high frequency resistance (HFR) values vs. temperature. The supercapacitor showed low to intermediate diffusion resistance from -40°C to 220°C (shaded region). The plots also display a diffusion-controlled charge-storage mechanism in the electrodes. The formation of the semi-circles observed in (a) signifies that a charge-transfer resistance may be present when decreasing the temperature at or below -50°C .

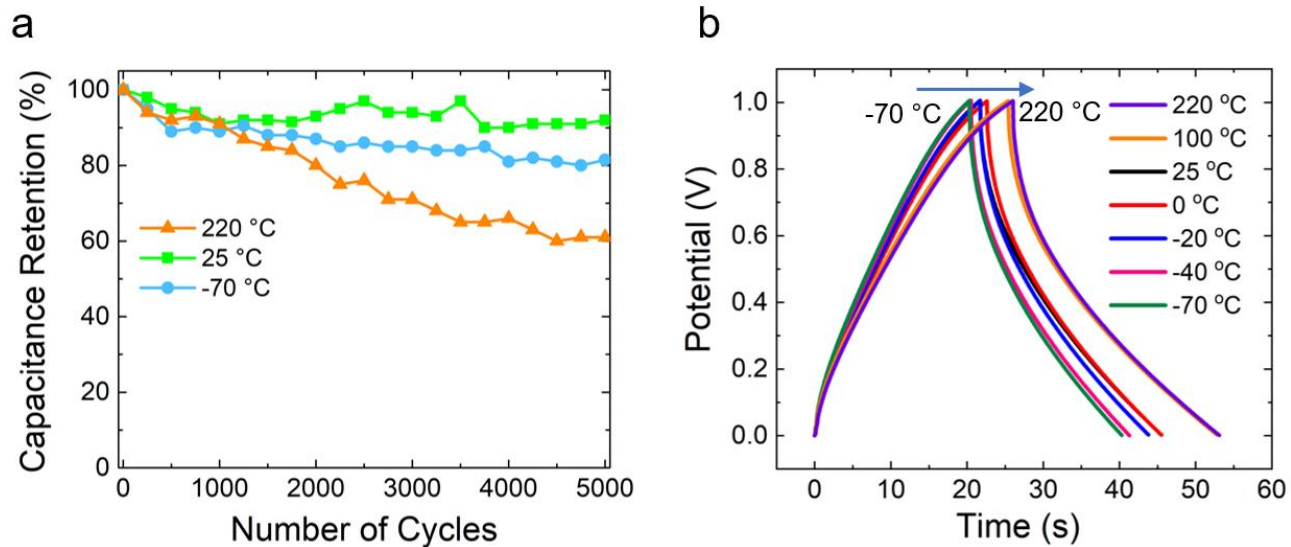


Figure 7. (a) Cycling stability of the device at -70 °C, 25 °C, and 220 °C after 5000 cycles. (b) Galvanostatic charge-discharge (GCD) curves at a current density of 1 mA cm^{-2} and at temperature ranges of -70 to 220 °C. The device was held for 1 hour at individual temperatures in the temperature range of -70 to 220 °C and the GCD was measured after the 1-hour exposure, at room temperature. The symmetrical shape of GCD plot is maintained even after exposing the device to extremely low (-70 °C) and high temperatures (220 °C).

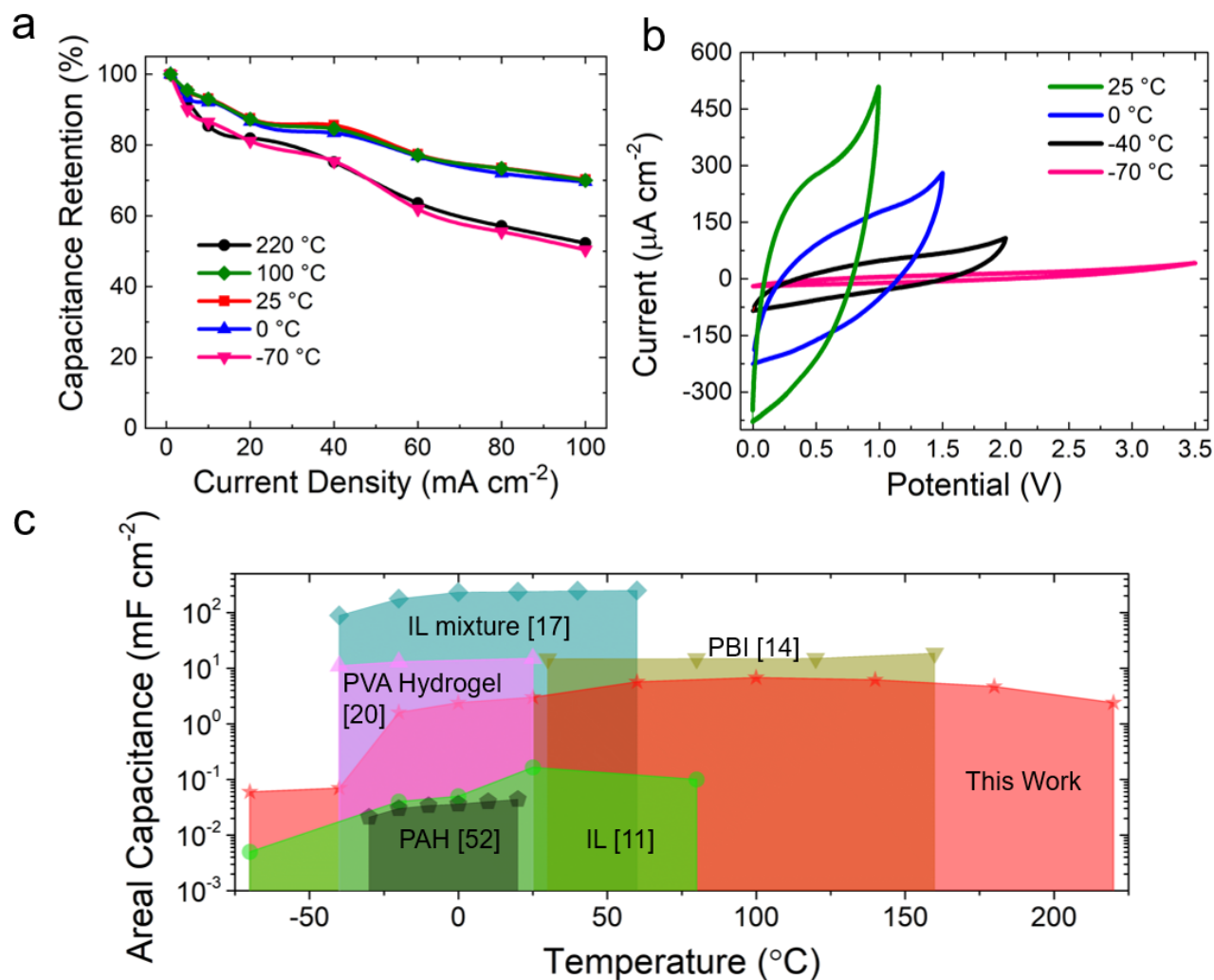


Figure 8. (a) Capacitance retention of the device as a function of different current densities at different temperatures. (b) CV curves show an increase in working potential window of the device from 1 to 3.5 V by decreasing the temperature from 25 to -70°C . (c) Comparison of areal capacitance vs. operating temperature range for this work with the literature data. The present work showed that the supercapacitor is working under a wide operating temperature ranges.

Graphical abstract

